The Impact of Slipper Microstructure on Slipper-Swashplate Lubrication Interface in Axial Piston Pump

JIHAI JIANG [ID]1, (Member, IEEE), ZEBO WANG [ID]1, AND GEQIANG LI [ID]2

1Harbin Institute of Technology, Harbin 150001, China
2Department of Mechanical and Electronic Engineering, Henan University of Science and Technology, Luoyang 471003, China

Corresponding author: Zebo Wang (wang_zebo@yeah.net)

ABSTRACT In order to decrease the tilt and eccentric abrasion of a slipper and improve the lubrication performance of the slipper-swashplate interface in an axial piston pump, this paper proposes a comprehensive numerical simulation method to predict the lubrication performance and designs three types of slipper microstructures such as micro-chamfering, micro-filleting and micro-stepping to improve the lubrication performance. The lumped-parameter numerical pressure-flow model of the axial piston pump and the lubrication model of the slipper-swashplate interface have been developed. These models consider the pressure of slipper's center oil pool, hydrostatic lubrication, hydrodynamic lubrication, slipper microstructures, slipper's micro motion and dynamic equilibrium. The influence of slipper microstructures on the lubrication performance of the slipper-swashplate interface has been profoundly studied. Simulation results demonstrate that the slipper without a microstructure leans forward and finally touches the swashpate leading to wear-out and that all the three types of slipper microstructures improve the lubrication performance, where the effects of micro-chamfering and micro-filleting are better than the effect of the micro-stepping. With the increase of the micro-chamfering depth, the leakage decreases and the friction power loss increases, while with the increase of the micro-chamfering depth, the leakage increases and the friction power loss decreases. The experimental results are essentially consistent with the simulation results, which confirms the numerical models feasible and effective. The current work is significant for further designs and the structural optimization of the slipper-swashplate interface.

INDEX TERMS Axial piston pump, eccentric abrasion, hydrodynamic lubrication, microstructure, slipper-swashplate interface.

I. INTRODUCTION

The hydraulic fluid power system is widely employed in modern industrial fields [1]. The swashplate type axial piston pump is the most common power hydraulic component. Owing to simple structure, compact design and high power density, it is widely applied in hydraulic transmission equipments, such as an excavator [2], an aircraft [3], a water hydraulic machine [4], [5] and a hydraulic transformer [6], etc. The axial piston pump is mainly composed of three interfaces, such as the slipper-swashplate interface,

the piston-cylinder interface [7] and the cylinder-valve plate interface [8]. The slipper-swashplate interface is the sliding interface between the rotating slipper and stationary swashplate as shown in Fig.1. The instantaneous pressure load of the entire displacement chamber, which periodically changes with the rotation of the main shaft, acts on the swashplate through the piston and slipper. The slipper sealing surface bears the periodic load. The pressurized oil of the displacement chamber flows into the slipper's center oil pool through the fixed damping holes of the piston and slipper. It produces a certain hydrostatic pressure to resist the slipper's external loads. The slipper-swashplate interface needs to simultaneously satisfy the functions of the bearing and sealing.

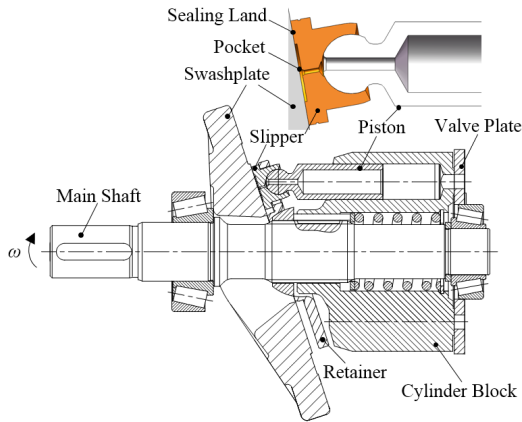The associate editor coordinating the review of this manuscript and approving it for publication was Hamid Mohammad-Sedighi [ID].

FIGURE 1. Diagram of main components and slipper-swashplate interface of axial piston pump.

FIGURE 2. Slipper's eccentric abrasion and failure picture.

Therefore, the certain oil film thickness needs to be formed to minimize the leakage and friction power loss for the sliding interface between the slipper and swashplate. The actual oil film thickness between the slipper and swashplate depends on the dynamically varying external loads of the slipper. The leakage [9], friction power loss and oil film thickness are hard to be detected in an actual pump. Canbulut et al. [10] applied an artificial neural network model to analyze the friction power loss of the slipper hydrostatic bearing. Sun et al. [11] investigated the relative position and friction power consumption between the retainer and the ball bowl of the slipper.

During the operation of the real axial piston pump, the slipper is found to have an eccentric abrasion and even a failure as seen in Fig. 2.

There are many factors resulting in the eccentric abrasion of the slipper, such as lubrication performance, oil film formation, temperature, motion posture and structure, etc.

Hooke et al. [12]–[16] investigated the influence of the compression coefficient, load pressure and damping hole's size on the lubrication performance of the slipper-swashplate interface. Bergada and Haynes [17]–[19] established a novel analytical model between slipper-swashplate interface, to analyze the variation of the lubrication characteristics on the bearing surface for slippers with the different size and position grooves.

Ma et al. [20] investigated the affecting factors of the oil film characteristics in the slipper pair using computational fluid dynamics. Kazama and Yamaguchi [21], [22] investigated the bearing characteristics and optimization design principles of the oil film at the slipper-swashplate interface in an axial piston pump. Ivantysynova and Schenk [23], [24] established the thermal elastohydrodynamic lubrication model of the slipper-swashplate interface, to analyze the thickness distribution, pressure distribution, temperature distribution and power loss of the oil film. Wieczorek and Ivantysynova [25] developed a CASPAR mathematical simulation tool, to predict the slipper's tilt and the oil film pressure distribution of the slipper-swashplate interface in an axial piston pump. Tang et al. [26]–[28] established a mathematical model of heat transfer, to predict the temperature distribution of the oil film in the slipper pair and the effect of temperature on the oil film characteristics.

Harris et al. [29] studied the tilt posture and lifting state of the slipper against the swashplate, and pointed out that the slipper might contact the swashplate owing to centrifugal torque at high speed. Xu et al. [30]–[33] investigated the tilt and slipper's rotational motion around its own axis and established a mathematical model for predicting the oil film thickness and pressure distribution.

Yu et al. [34], [35] investigated the application of the hydrostatic balance slipper in a water axial piston pump. Nie et al. [4], [5] proposed a slipper structure with an annular damping hole for the water axial piston pump. Wondergem [36] researched the impact of piston micro-surface shaping on leakage, axial friction force and energy dissipation of piston/cylinder interface of axial piston machines.

Previous research just focuses on the investigation and modeling the lubrication between the slipper and swashplate. However, a comprehensive numerical simulation method and the impact of the slipper sealing surface microstructure on the lubrication performance has yet to be published focusing specifically on the slipper-swashplate interface.

Fig. 3 shows the proposed comprehensive simulation method to predict the lubrication performance of the slipper-swashplate interface. The flow-pressure model of the axial piston pump is established according to the operating conditions and geometric models with a lumped parameter method. Then the pressure model of the slipper's center oil pool and the lubrication model of the slipper-swashplate interface are developed. The coupling solver among the model of the slipper's center oil pool pressure, lubrication model and dynamic balance equations is constructed using OpenFoam. Further, three types of slipper microstructures are designed to improve the lubrication performance of the slipper-swashplate interface. Finally, the friction power losses of the slipper-swashplate interface with different micro-chamfering widths are measured by experiments.
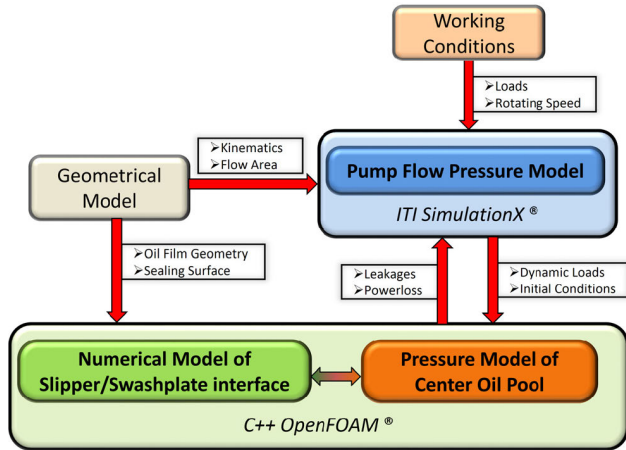
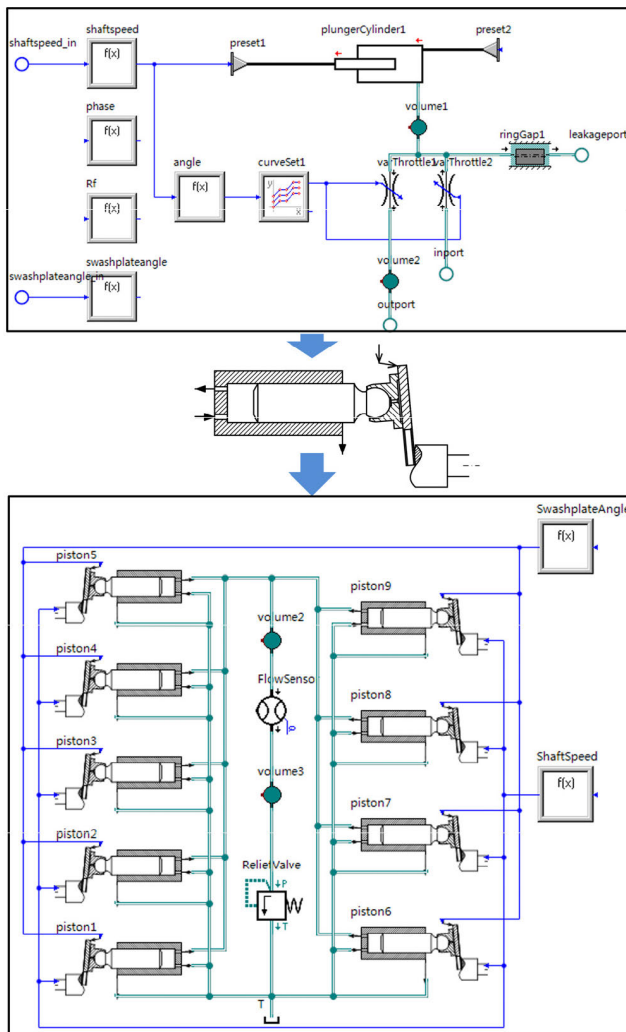**FIGURE 3.** Comprehensive simulation method for lubrication performance of slipper-swashplate interface.

FIGURE 4. Flow-pressure simulation model of axial piston pump.

II. DYNAMIC PRESSURE OF DISPLACEMENT CHAMBER

The flow pressure simulation model of the axial piston pump is constructed using the SimulationX tool, as shown in Fig. 4.
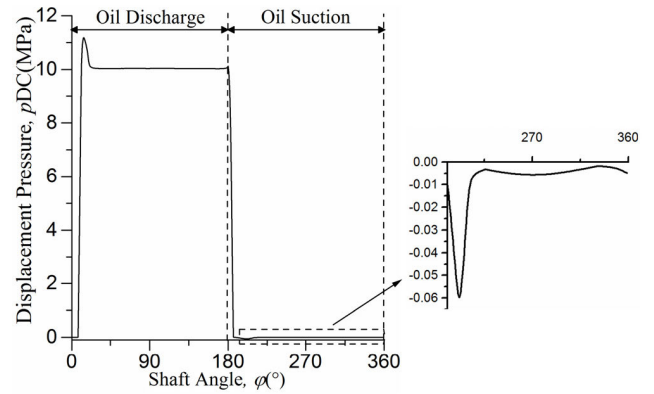

FIGURE 5. Dynamic pressure of displacement chamber.

It is assumed that the oil suction and discharge processes of the axial piston pump periodically vary. The control volume of the displacement chamber in the cylinder block is connected with the oil suction and discharge waist grooves of the valve plate, respectively. The flow section areas of the oil passage windows are determined by the structure of the valve plate and the rotation of shaft. A single piston model is established firstly, and after compounding it as a new component, the flow pressure simulation model of the whole pump is built.

The dynamic pressure in displacement chamber p_{DC} is described as follow:

$$\frac{dp_{DC}}{dt} = \frac{K}{V_{DC}}\left[-\frac{dV_{DC}}{dt} - \left(Q_{HP} + Q_{LP} + Q_{leakage}\right)\right] \quad (1)$$

where K is the oil's bulk elastic modulus; V_{DC} is the instantaneous volume of displacement chamber; $Q_{leakage}$ is the leakage from displacement chamber, which includes leakage from slipper-swashplate interface, piston-cylinder interface and cylinder-valve plate interface; Q_{HP} and Q_{LP} are the flow from high pressure port and low pressure port to control volume, which are calculated based on the orifice flow equation. Q_{HP} and Q_{LP} can be described as:

$$Q_{HP} = C_d A_{HP}\sqrt{\frac{2}{\rho}\left(p_{DC} - p_{HP}\right)} \quad (2)$$

$$Q_{LP} = C_d A_{LP}\sqrt{\frac{2}{\rho}\left(p_{DC} - p_{LP}\right)} \quad (3)$$

where C_d is the flow coefficient; ρ is the oil density; A_{HP} and A_{LP} are the flow area between displacement and high and low pressure port; p_{HP} and p_{LP} are the pressure of high and low pressure port.

The flow pressure simulation model of the axial piston pump is solved to obtain the dynamic pressure of the displacement chamber in one cycle, as shown in Fig. 5. The shaft angle range of $0°\sim180°$ is the oil discharge stage of the pump, called the high-pressure area; the angle range of $180°\sim360°$ is the oil suction stage of the pump, called the low-pressure area.
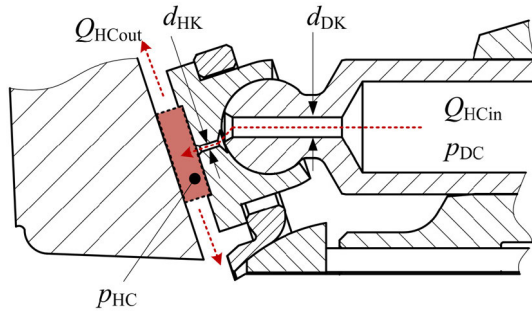
FIGURE 6. Control volume of slipper's center oil pool.

When the piston begins to enter the high-pressure area, there exists the positive overshoot of pressure. Because the high-pressure oil of the waist groove pours into the displacement chamber through the triangular groove, when the piston passes through a triangular groove transition area before completely entering the oil discharge area. Moreover, the axial movement of the piston causes the displacement chamber's volume compression. Similarly, when the piston begins to enter the low-pressure area, the negative overshoot of pressure occurs, which causes the displacement chamber's high-pressure oil to flow into the waist groove in the oil suction area through the triangular groove. Additionally, the reverse axial movement of the piston causes the displacement chamber's volume expansion.

III. LUBRICATION MODEL OF SLIPPER-SWASHPLATE INTERFACE AND ALGORITHM

In the axial piston pump, the slipper is periodically loaded by the oil pressure from the displacement chamber. In addition, it is also a periodic motion for the slipper relative to the swashplate. As long as the lubrication performance indexes of one slipper-swashplate interface are calculated, those of the other ones can be obtained according to the phase difference between slippers. The lubrication performance indexes mainly includes the oil film thickness, the friction power loss and the leakage, etc. This section researches and develops the lubrication model of a single slipper-swashplate interface.

A. PRESSURE MODEL OF SLIPPER'S CENTER OIL POOL

As the pressure of the slipper's center oil pool plays a decisive role in the hydrostatic supporting force, the pressure distribution of the center oil pool should be calculated. The depth of the slipper's center oil pool is 0.7-1.0 mm. Therefore, the pressure of the entire oil pool is considered to be uniform. As shown in Fig. 6, the slipper's center oil pool is regarded as the control volume.

Considering the compressibility of the oil in the control volume, the pressure equation is expressed as:

$$\frac{dp_{HC}}{dt} = \frac{K}{V_{HC}}\left(Q_{HCin} - Q_{HCout} - \frac{dV_{HC}}{dt}\right) \quad (4)$$

where p_{HC} is the pressure of the slipper's center oil pool; K is the oil's bulk elastic modulus; Q_{HCin} is the flow from the displacement chamber through the damping holes and

into the slipper's center oil pool; Q_{HCout} is the flow from the slipper's center oil pool to the pump house through the gap between the slipper and the swash plate; V_{HC} is the fluid control volume of the slipper's center oil pool.

The damping holes in the slipper and piston are circular tube-type ones, and the damping hole diameter is very small ($d < 1$ mm). The length to diameter ratio is generally less than 100 ($l/d < 100$), and the flow is essentially laminar flow. Therefore, the effect of the laminar flow starting section should be considered. Owing to a sharp edge of the inlet in the damping hole, effects of the inlet shrinkage and expansion loss are regarded as those of the laminar flow starting section. The flow equation is expressed as:

$$Q_{HCin} = \frac{C_A}{C_q}(p_{DC} - p_{HC}) \quad (5)$$

where

$$C_A = \frac{\pi}{128\mu} \cdot \frac{d_{DK}^4 d_{HK}^4}{l_{DK}d_{HK}^4 + l_{HK}d_{DK}^4}$$

$$C_q = \frac{1}{64}\left[\frac{d_{HK}R_e}{l_{HK}} + 64 + 3\left(\frac{d_{HK}R_e}{l_{HK}}\right)^{0.75}\right]$$

where R_e is the Reynolds number; C_A is the flow coefficient of the damping hole; C_q is the flow correction coefficient of the damping hole; μ is the oil's dynamic viscosity; l_{DK} and l_{HK} are the length of the damping holes of the piston and slipper, respectively; d_{DK} and d_{HK} are the diameter of the damping holes of the piston and slipper, respectively.

The flow from the slipper's center oil pool into the pump house through the clearance between the slipper and swashplate is obtained by integrating the fluid's radial velocity component along the oil film thickness and outer circumference directions, as follows:

$$Q_{HCout} = \int_0^{2\pi}\int_0^h v_r r\,dz\,d\theta = \int_0^{2\pi}\left[-\frac{h^3}{12\mu}\cdot\frac{\partial p}{\partial r} + \frac{h}{2}v\right]r_{HSout}\,d\theta \quad (6)$$

where h is the oil film thickness; v_r is the radial velocity component of the fluid in the oil film; v is the linear velocity at any point on the sealing surface of the slipper; r_{HSout} is the outer diameter of the sealing surface of the slipper.

B. PRESSURE MODEL OF OIL FILM

During the pump's operation, the slipper's micro-motion depends on the dynamically periodically varying loads from the displacement chamber. The resisting forces and external loads of the slipper-swashplate interface need to keep dynamic equilibrium. Fig. 7 defines the control points describing the slipper's micro-motion.

The points H_1, H_2 and H_3 with an interval of 120° are located on the slipper's outer diameter circumference, and their oil film thickness values are h_1, h_2 and h_3, respectively. Point H_1 is on the y_H axis. The points H_1, H_2 and H_3 are used to describe the variation of the slipper posture, such
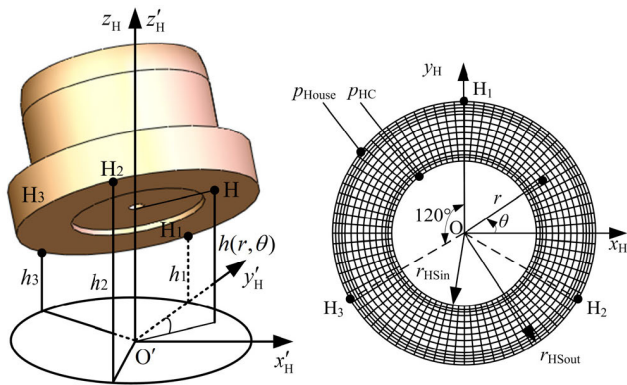
FIGURE 7. Definition of control points describing slipper's micro motion.

as the translational motion along the axis z_H, which is the direction perpendicular to the plane of the swashplate, and the rotational motion around the x_H and y_H axes. The oil film thickness caused by the slipper's micro motion at any point on the slipper bottom plane is expressed as:

$$h(r, \theta) = \frac{r \sin \theta}{3 r_{\text{HSout}}}(2h_1 - h_2 - h_3) + \frac{r \cos \theta}{\sqrt{3} r_{\text{HSout}}}(h_2 - h_3) + \frac{1}{3}(h_1 + h_2 + h_3) \quad (7)$$

Similarly, the vertical velocity components of three points located on the slipper's outer circumference are used to describe the extrusion rate of the oil film, which is caused by the slipper's micro-motion, at any point on the slipper bottom plane, as follows:

$$\frac{\partial h(r, \theta)}{\partial t} = \frac{r \sin \theta}{3 r_{\text{HSout}}}(2\frac{dh_1}{dt} - \frac{dh_2}{dt} - \frac{dh_3}{dt}) + \frac{r \cos \theta}{\sqrt{3} r_{\text{HSout}}} \times (\frac{dh_2}{dt} - \frac{dh_3}{dt}) + \frac{1}{3}(\frac{dh_1}{dt} + \frac{dh_2}{dt} + \frac{dh_3}{dt}) \quad (8)$$

where r is the distance from any point on the slipper bottom plane to the center point O; θ is the angle between the line from any point on the slipper bottom plane to the center point O and x_H axis.

The two-dimensional grid diagram of the oil film shape of the slipper-swashplate interface is shown in Fig. 7 (right). The inner boundary is the wall of the slipper's center oil pool, and the outer boundary is the pump house. By increasing the grid density at the inner and outer boundaries, the influence of the sealing surface microstructure on the oil film can be more accurately captured.

Considering that the magnitude of the oil film thickness between the slipper and swashplate is at micron level, the fluid is assumed as an incompressible Newtonian fluid and the fluid flow is considered as the lamina flow. The Reynolds equation of the slipper-swashplate interface is derived as:

$$\nabla \cdot \left(-\frac{h^3}{12\mu} \cdot \nabla p \right) - \frac{v}{2} \cdot \nabla h + \frac{\partial h}{\partial t} = 0 \quad (9)$$

where the first term is the differential pressure flow term of the fluid. The second term is the shear flow term of the fluid
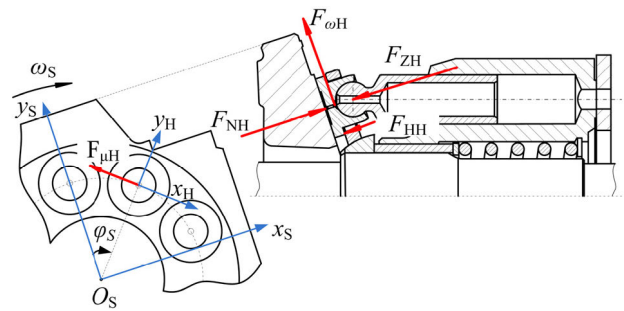
and also the cause of the hydrodynamic effect. The third term is the extrusion motion term of the fluid. When the slipper slightly moves, the extrusion rate plays a decisive role in the generation of the oil film's dynamic pressure. p is the pressure at any point on the slipper bottom plane.

The velocity boundary condition on the oil film between the slipper and swashplate interface can be described as:

$$\begin{cases} v_r(z = h) = v_{Hr} \\ v_\theta(z = h) = v_{H\theta} \end{cases}, \quad \begin{cases} v_r(z = 0) = 0 \\ v_\theta(z = 0) = 0 \end{cases} \quad (10)$$

where v_θ is the circumferential velocity component of the fluid in the oil film; v_{Hr} and $v_{H\theta}$ are the radial and circumferential velocity component of the point on the slipper bottom plane.

The friction stress between the slipper and swashplate interface can be expressed as:

$$\begin{cases} \tau_{Hr} = \frac{h}{2} \frac{\partial p}{\partial r} + \mu \frac{v_{Hr}}{h} \\ \tau_{H\theta} = \frac{h}{2} \frac{\partial p}{r \partial \theta} + \mu \frac{v_{H\theta}}{h} \end{cases} \quad (11)$$

where τ_{Hr} and $\tau_{H\theta}$ are the radial and circumferential component of the friction stress.

The friction power loss between the slipper and swashplate interface can be written as:

$$W_{\text{Friction}} = \int_0^{2\pi} \int_{r_{\text{HSin}}}^{r_{\text{HSout}}} (\tau_{Hr} v_{Hr} + \tau_{H\theta} v_{H\theta}) \, r dr d\theta \quad (12)$$

C. DYNAMIC SLIPPER MODEL

The dynamic analysis of the slipper is shown in Fig. 8.

When the pressure in the displacement chamber is built up, the oil film between the slipper and swashplate produces a supporting reaction force to resist the external loads exerted on the slipper. The mass and inertia of the slipper are very small and can be ignored. Hence, the dynamic balance equations of the slipper are expressed as:

$$\begin{cases} F_{NH} - F_{ZH} - F_{HH} = 0 \\ M_{p_H x_H} + M_{\omega H} = 0 \\ M_{p_H y_H} + M_{\mu x_H} = 0 \end{cases} \quad (13)$$

where F_{ZH} is the main load of the slipper, composed of the displacement chamber's pressure, friction force between the piston and cylinder block and the inertia force of the
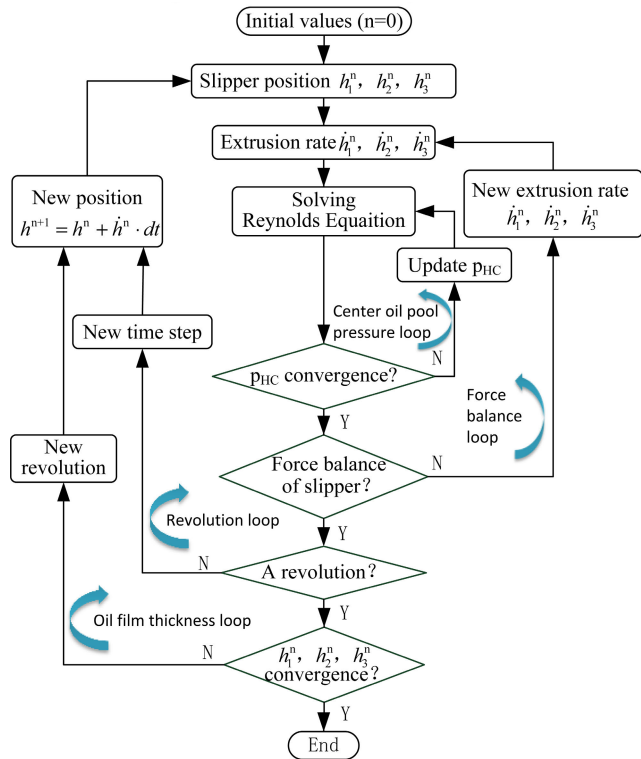

FIGURE 8. Diagram of dynamic slipper's analysis.

FIGURE 9. Block diagram of flow field solution algorithm.

FIGURE 10. Distribution of oil film thickness without microstructure.

cycles satisfy the convergence condition. In other words, all these differences are less than $1 \times 10^{-8} \mu$m.

IV. ANALYSIS OF SIMULATION RESULTS

Both the pump house and inlet pressure are set to 0.1 MPa. The operating pressure is 10 MPa. The main shaft speed is 1500 r/min. The swashplate is angle 18°. The other relevant parameters from the real pump (A10VSO45) used in simulation are listed in Table 1.

TABLE 1. Relevant parameters used in simulation.

Symbol	Value	Unit
r_{HSin}	5.9	mm
r_{HSout}	10.7	mm
l_{HK}	2.9	mm
d_{HK}	0.8	mm
l_{DK}	13.9	mm
d_{HDK}	2.5	mm
μ	0.02784	N·s/m^2
K	2	GPa

piston-slipper assembly; F_{HH} is the compressing force acted on the slipper from the retainer or spring; F_{NH} is the supporting reaction force acted on the slipper, composed of hydrostatic pressure and hydrodynamic pressure of the oil film; $M_{\omega H}$ is the centrifugal moment of the slipper; $M_{\mu H}$ is the friction moment of the slipper; M_{pHxH} and M_{pHyH} are the moments generated by the oil film pressure relative to the x_H and y_H axes, respectively.

Although the oil film extrusion rate does not directly appear in the slipper's dynamic balance equations, it causes the oil film to produce an extrusion effect and directly affects the oil film pressure distribution. Therefore, it changes the supporting force acted on the slipper to adjust the slipper's posture and leads it to regain balance.

D. SOLUTION ALGORITHM

According to the above description of the models of the slipper-swashplate interface, the block diagram of the flow field solution algorithm is shown in Fig. 9.

By solving the inner pressure calculation loop of the slipper's center oil pool, the center oil pool pressure and the corresponding oil film pressure distribution are obtained. Then, the dynamic balance calculation loop of the slipper is used to calculate the thickness and extrusion rate distribution of the oil film at this shaft angle under the new balance. The shaft angle step is 1°. Every time the numerical simulation model runs for one cycle (360°), the convergence of the oil film thickness is checked until all the oil film thickness differences at the same shaft angle between the adjacent two
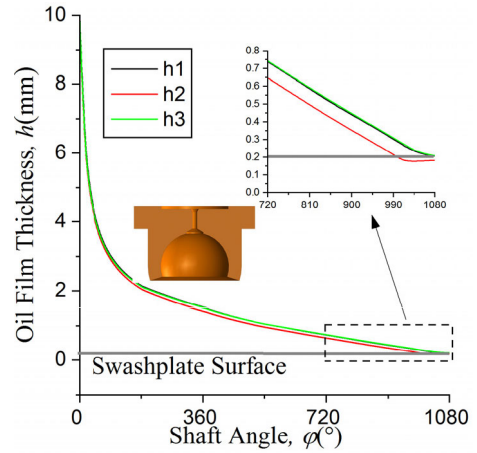
A. INFLUENCE OF MICROSTRUCTURE ON OIL FILM

The distribution of the oil film thickness without a microstructure is shown in Fig. 10.

By considering the positions of the points H_1, H_2, and H_3 (Fig. 7), Fig. 10 shows that the slipper has a forward leaning posture ($h_2 < h_1, h_3$), and finally contacts the swashplate resulting in eccentric abrasion. The reason is that the direction of the convergence port of the wedge-shaped oil film formed by the forward leaning posture and the direction of the relative motion speed of the slipper and swashplate are the same. Therefore, the wedge-shaped oil film does not satisfy the required conditions to generate a dynamic pressure effect. To avoid the contact abrasion between the slipper and the swashplate, a particular oil film should be formed to ensure the lubrication of the slipper-swashplate interface. According to the formation conditions of the hydrodynamic effect, three types of slipper microstructures for the sealing surface are designed, namely, micro-chamfering, micro-filleting and micro-stepping, as shown in Fig. 11.
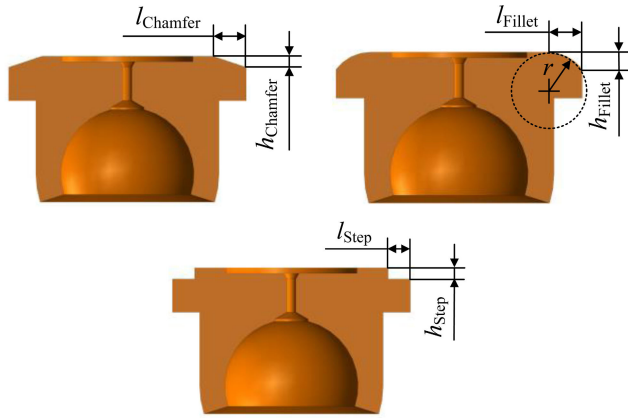
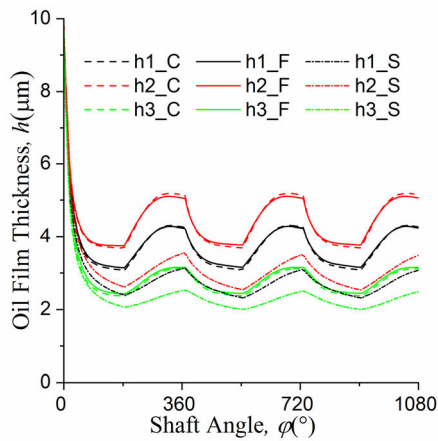**FIGURE 11.** Slippers with three different microstructures.

FIGURE 12. Oil film thickness distribution with different microstructures.

FIGURE 13. Oil film pressure distribution with different microstructures at main shaft angle of 45°.

For three types of microstructures with the same processing parameters, such as depth ($h = 10\ \mu\text{m}$) and width ($l = 0.5$ mm), the lubrication models are solved to obtain the oil film thickness distribution as shown in Fig. 12, where C, F, S are the micro-chamfering, micro-filleting and micro-stepping, respectively.

As shown in Fig. 12, all three types of microstructures cause the slipper-swashplate interface to form a particular oil film, and the slipper exhibits a backward tilt posture ($h_2 > h_1$, h_3). The wedge-shaped oil film formed by the backward tilt posture of the slipper converges in the opposite direction of the slipper and swashplate's relative movement direction. This wedge-shaped oil film satisfies the required conditions to generate a dynamic pressure effect. The oil film pressure distribution at the main shaft angle of 45° in the oil discharge area is shown in Fig. 13.

The backward tilt posture of the slipper produces the dynamic pressure (Fig. 13) in the oil film to improve its supporting capacity. This dynamic pressure is helpful to form the oil film between the slipper and swashplate. The simulation results demonstrate that the influences of the micro-chamfering and micro-filleting on the oil film thickness of the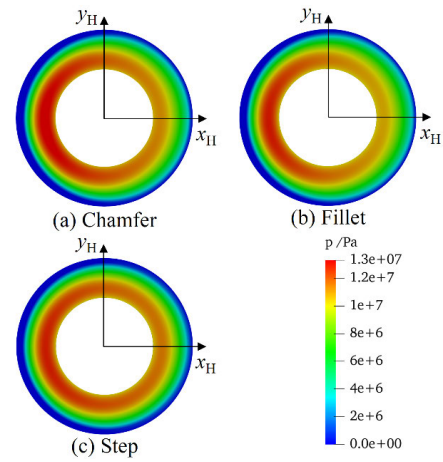 slipper-swashplate interface are essentially equivalent, and greater than those of the micro-stepping on the oil film thickness.

B. INFLUENCE OF MICROSTRUCTURE ON LEAKAGE AND FRICTION POWER LOSS

The visual expression of the influence of microstructures on the oil film thickness is the leakage and friction power loss of the slipper-swashplate interface. Different micro-chamfering depths and widths are listed in Table 2.

TABLE 2. Different micro-chamfering depths and widths.

Depth	Width	l_{Chamfer} (mm)		
		0.5	1.0	1.5
	10	C0.5-10		
h_{Chamfer} (µm)	15	C0.5-15		
	20	C0.5-20	C1.0-20	C1.5-20

The leakage flow and friction power loss of the slipper-swashplate interface with different micro-chamfering depths and widths are shown in Fig. 14, where P and Q are the friction power loss and leakage flow, respectively.

As shown in Fig. 14(a), with the increase of the micro-chamfering depth, the leakage flow decreases, while the friction power loss increases. Because the hydrodynamic effect becomes weak, leading the oil film thickness to be thin. Similarly, as can be seen in Fig. 14(b), with the increase of the micro-chamfering width, the leakage flow increases, while the friction power loss decreases. The reason is that the hydrodynamic effect becomes strong leading the oil film thickness to be thick. By comparing the differences from P_C0.5-10 to P_C0.5-20 with from P_C0.5-20 to P_C1.5-20, as seen in Fig. 13, it is obviously found that the micro-chamfering width has a greater influence on the oil film than the micro-chamfering depth.

V. EXPERIMENTS
Fig. 15 (a) and (b) show the schematic diagram and physical picture of the test rig for the friction power loss of the slipper-swashplate interface, respectively.
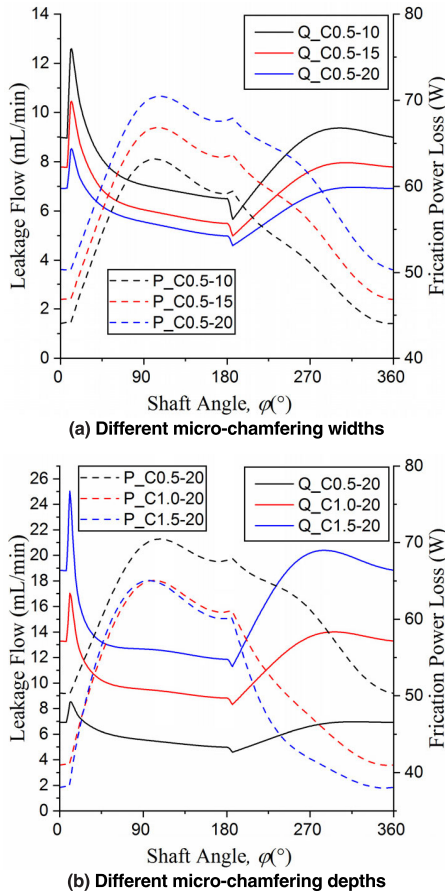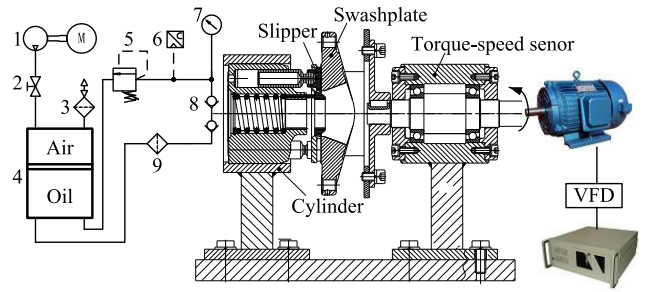
(a) Different micro-chamfering widths

(b) Different micro-chamfering depths

FIGURE 14. Leakage flow and friction power loss with different micro-chamfering depth and width. The solid line indicates leakage flow; the dotted line indicates friction power loss.

1 – Air compressor, 2 – Cut-off valve, 3 – Pre-pressure air filter, 4 – Closed tank with piston, 5 – Relief valve, 6 – Pressure senor, 7 – Pressure meter, 8 – Check valve, 9 – Filter
(a) Schematic diagram
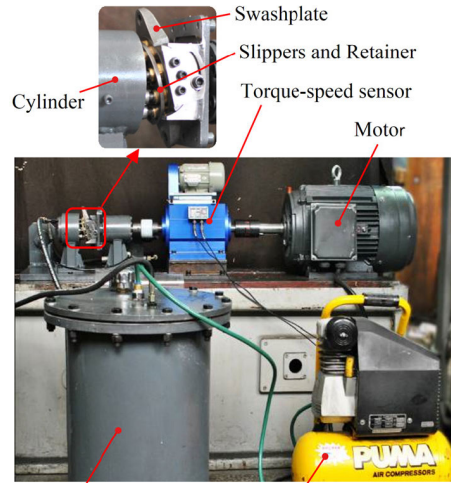
(b) Physical picture

FIGURE 15. Test rig for friction power loss of slipper-swashplate interface.

The test rig for the friction power loss of the slipper-swashplate interface is mainly composed of experimental pump, variable frequency converter, motor, torque-speed sensor, check valve, relief valve, pressurized oil tank, air compressor and industrial computer. Through an inverse kinematics method, the simulation or real pump (A10VSO45) is redesigned to the experimental pump, where the relative kinematics between the slipper and swashplate can be simulated. The experimental pump still has nine slippers, the same as the real pump. With the swashplate's rotation and the help of the retainer or spring force, the piston does the reciprocating linear motion to make the volume of the piston chamber change periodically so that the experimental pump can realize the function of oil suction and discharge. The test interference of the cylinder-valve plate interface to the slipper-swashplate interface can be effectively eliminated by replacing the valve plate with two check valves. Reasonable experimental steps can eliminate the test interference of the piston-cylinder interface, so as to measure the friction power loss between the slipper and swashplate. The experimental steps are as follows.

Step 1, the torque-speed sensor is not connected to the experimental pump. The data measured by the torque-speed sensor is the idling power loss of the motor, W_{Motor}.

Step 2, the torque-speed sensor is connected to the experimental pump. The relief valve pressure and the swashplate angle are set to 0 MPa and 0°, respectively. The data ($W_{\mathrm{Rig\_0°}}$) measured by the torque-speed sensor includes the idling power loss (W_{Motor}) of the motor and the power loss ($W_{\mathrm{Slipper\_0°}}$) of the slipper-swashplate interface under the spring force, as follows:

$$W_{\mathrm{Slipper\_0°}} = W_{\mathrm{Rig\_0°}} - W_{\mathrm{Motor}} \qquad (14)$$

According to the mechanics mechanism, it is easy to compute the power loss ($W_{\mathrm{Slipper\_18°}}$) of the slipper-swashplate interface under the spring force at the swashplate angle of 18°, which is the same as the swashplate angle of the simulation pump, as follows:

$$W_{\mathrm{Slipper\_18°}} = \frac{W_{\mathrm{Slipper\_0°}}}{\cos 18°} \qquad (15)$$

Step 3, the swashplate angle of the experimental pump is set to 18°. The pressure of the piston chamber is still 0 MPa. The load acted on the slipper is only the retainer or spring force. The data ($W_{\mathrm{Rig\_18°}}$) measured by the torque-speed sensor includes the idling power loss (W_{Motor}) of the motor, the power loss of the piston-cylinder interface ($W_{\mathrm{Piston\_18°}}$)

TABLE 3. Average friction power loss with different micro-chamfering widths.

Micro-chamfering	Average friction power loss (W)	
	Experiment	Simulation
C0.5-20	72.276	62.021
C1.0-20	66.816	56.935
C1.5-20	65.296	55.727

and the slipper-swashplate interface under the spring force ($W_{\text{Slipper\_18°}}$). The sum (W_{PM}) of the power loss of the piston-cylinder interface and the idling power loss of the motor is written as:

$$W_{\text{PM}} = W_{\text{Piston\_18°}} + W_{\text{Motor}} = W_{\text{Rig\_18°}} - W_{\text{Slipper\_18°}}$$

(16)

Step 4, the relief valve pressure is set to be the same as the working pressure of the simulation pump. The data (W_{Rig}) measured by the torque-speed sensor includes the idling power loss (W_{Motor}) of the motor, the power loss of the piston-cylinder interface and the slipper-swashplate interface (W_{Slipper}). This power loss of the piston-cylinder interface can be considered to be approximately equal to that one from step 3. The reason for this is that the power loss of the piston-cylinder interface is little affected by the pressure of the piston chamber. The power loss of the slipper-swashplate interface can be described as:

$$W_{\text{Slipper}} = W_{\text{Rig}} - W_{\text{MP}}$$

(17)

To sum up, the first three steps are preparation before the power loss measurement of the slipper-swashplate interface in the experimental pump. The data of the first three steps are integrated in the data acquisition program. The friction power loss of the single slipper-swashplate can be obtained by dividing the power loss measured in step 4 by the number of slippers in the experimental pump.

Switching frequency of check valves limits the rotation speed of the main shaft. When the rotation speed is 1500 r/min, which is the same as that of the simulation pump, the pressure sampling value is relatively stable. Under the same working conditions of the simulation models, the friction power losses of the single slipper-swashplate interface with three different micro-chamfering widths have been measured by experiments. After the stable operation of the experimental platform, the experimental results within 20 seconds are shown in Fig. 16(a). The simulation results for the friction power loss of the single slipper-swashplate interface in one cycle (360°) are presented in Fig. 16(b).

As seen in Fig. 16(a) and (b), both the experimental and simulation results show that the friction power loss of the slipper-swashplate interface decreases with the increase of the micro-chamfering width.

The average friction power losses of the single slipper-swashplate interface with different micro-chamfering widths are shown in Table 3.
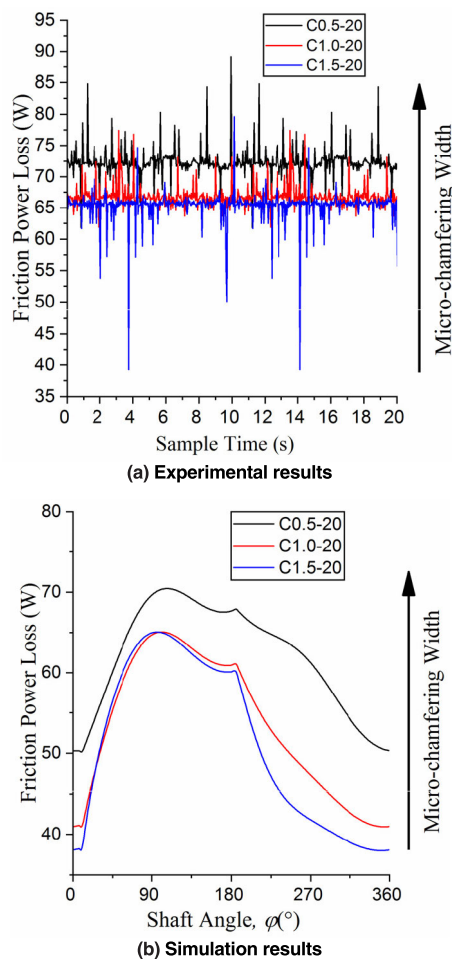

FIGURE 16. Comparison of experimental and simulation results of friction power loss of the single slipper-swashplate interface with different micro-chamfering widths.

As seen in Table 3, the experimental results are slightly higher than the simulation results. The reason for this is that the slipper's rotational motion around its own axis is not copied into the experimental pump. This rotation can generate the hydrodynamic effect to form a better oil film, which reduces the friction power loss between the slipper and swashplate. As shown in Table 3, the average friction power loss with C1.5-20 micro-chamfering decreases 9.66% comparing with the one with C0.5-20 micro-chamfering. The experimental results are essentially consistent with the simulation results.

VI. CONCLUSION

In order to predict and improve the lubrication performance of the slipper-swashplate interface in the axial piston pump, the comprehensive numerical simulation method and three types of slipper microstructures are proposed. According to the numerical simulation and experimental results, several conclusions are obtained as follow:

(1) The simulation results demonstrate that the slipper without a microstructure overturns and finally touches the swashpate, resulting in eccentric abrasion.

(2) The simulation results indicate that all three types of microstructures are conducive to the formation of the oil film lubrication. The improvements of the micro-chamfering and micro-filleting on the lubrication performance of the slipper-swashplate interface are obvious and better than that of the micro-stepping.

(3) The simulation results show that the leakage flow decreases and friction power loss increases with the increase of the micro-chamfering depth. In contrast, the leakage flow increases and friction power loss decreases with the increase of the micro-chamfering width.

(4) The average friction power loss of the slipper-swashplate interface with C1.5-20 decreases 9.66% comparing with the power loss with C0.5-20. The experimental results have good consistency with the simulation results. The comprehensive numerical simulation method presented is proved to be feasible and effective for predicting the lubrication performance of the slipper-swashplate interface.

The future work of this study will optimize the structure parameters of the slipper sealing surface and take the thermal effect into account in the lubrication model of the slipper-swashplate interface.

REFERENCES

[1] W. Wu and C. Yu, "Simulation and experimental analysis of hydraulic directional control for displacement controlled system," *IEEE Access*, vol. 6, pp. 27993–28000, 2018, doi: 10.1109/ACCESS.2017.2777958.

[2] P. Casoli, L. Riccò, and D. Cesare, "Modeling and verification of an excavator system—Axial piston pump, kinematics and load sensing flow sharing valve block," in *Proc. SICFP*, Linköping, Sweden, 2013, pp. 53–63.

[3] S. Guo, J. Chen, Y. Lu, Y. Wang, and H. Dong, "Hydraulic piston pump in civil aircraft: Current status, future directions and critical technologies," *Chin. J. Aeronaut.*, vol. 33, no. 1, pp. 16–30, Jan. 2020, doi: 10.1016/j.cja.2019.01.013.

[4] S. L. Nie, G. H. Huang, and Y. P. Li, "Tribological study on hydrostatic slipper bearing with annular orifice damper for water hydraulic axial piston motor," *Tribol. Int.*, vol. 39, no. 11, pp. 1342–1354, 2006, doi: 10.1016/j.triboint.2005.10.007.

[5] S. L. Nie, Q. M. Jiao, and Z. Y. Yu, "A new type of hydrostatic slipper bearing and its application to water hydraulic motor," *Mech. Sci. Tech.*, vol. 23, no. 7, pp. 777–779, 2006.

[6] W. Shen and J. Wang, "An integral terminal sliding mode control scheme for speed control system using a double-variable hydraulic transformer," *ISA Trans.*, 2019, doi: 10.1016/j.isatra.2019.08.068.

[7] J. Jihai, W. Kelong, W. Zebo, and S. Yi, "The impact of bushing thickness on the piston/cylinder interface in axial piston pump," *IEEE Access*, vol. 7, pp. 24971–24977, 2019, doi: 10.1109/ACCESS.2019.2900668.

[8] J. Jihai and Y. Weipeng, "An approach to predict wear distribution of valve plate in elasto-hydrodynamic lubrication," *IEEE Access*, vol. 7, pp. 86789–86797, 2019, doi: 10.1109/ACCESS.2019.2923545.

[9] H. Tang, W. Yang, and Z. Wang, "A model-based method for leakage detection of piston pump under variable load condition," *IEEE Access*, vol. 7, pp. 99771–99781, 2019, doi: 10.1109/ACCESS.2019.2930816.

[10] F. Canbulut, Ş. Yildirim, and C. Sinanoğlu, "Design of an artificial neural network for analysis of frictional power loss of hydrostatic slipper bearings," *Tribol. Lett.*, vol. 17, no. 4, pp. 887–899, Nov. 2004.

[11] Y. Sun, Y. Li, and J. H. Jiang, "Stress analysis and experiments for slipper retainer and ball guide in axial piston pump," *J. Xian Jiaotong Univ.*, vol. 47, no. 2, pp. 103–108, 2013, doi: 10.7652/xjtuxb201302018.

[12] E. Koç and C. J. Hooke, "Investigation into the effects of orifice size, offset and overclamp ratio on the lubrication of slipper bearings," *Tribol. Int.*, vol. 29, no. 4, pp. 299–305, Jun. 1996.

[13] E. Koç and C. J. Hooke, "Considerations in the design of partially hydrostatic slipper bearings," *Tribol. Int.*, vol. 30, no. 11, pp. 815–823, Nov. 1997, doi: 10.1016/S0301-679X(97)00064-9.

[14] K. Y. Li and C. J. Hooke, "A note on the lubrication of composite slippers in water-based axial piston pumps and motors," *Wear*, vol. 147, no. 2, pp. 431–437, Jul. 1991.

[15] C. J. Hooke and K. Y. Li, "The lubrication of overclamped slippers in axial piston pumps—Centrally loaded behaviour," *Proc. Inst. Mech. Eng., C, J. Mech. Eng. Sci.*, vol. 202, no. 4, pp. 287–293, Jul. 1988.

[16] C. J. Hooke and K. Y. Li, "The lubrication of slippers in axial piston pumps and motors—The effect of tilting couples," *Proc. Inst. Mech. Eng., C, J. Mech. Eng. Sci.*, vol. 203, no. 5, pp. 343–350, Sep. 1989.

[17] S. Kumar, J. M. Bergada, and J. Watton, "Axial piston pump grooved slipper analysis by CFD simulation of three-dimensional NVS equation in cylindrical coordinates," *Comput. Fluids*, vol. 38, no. 3, pp. 648–663, Mar. 2009, doi: 10.1016/j.compfluid.2008.06.007.

[18] J. M. Bergada, J. M. Haynes, and J. Watton, "Leakage and groove pressure of an axial piston pump slipper with multiple lands," *Tribol. Trans.*, vol. 51, no. 4, pp. 469–482, Jul. 2008, doi: 10.1080/10402000802044332.

[19] J. M. Bergada, J. Watton, J. M. Haynes, and D. L. Davies, "The hydrostatic/hydrodynamic behaviour of an axial piston pump slipper with multiple lands," *Meccanica*, vol. 45, no. 4, pp. 585–602, Aug. 2010, doi: 10.1007/s11012-009-9277-0.

[20] J. M. Ma, Y. Y. Shen, and Q. L. Li, "Oil film analysis of swash plate/slipper pair based on CFD," *J. Beijing Univ. Aeronaut. Astronaut.*, vol. 42, no. 2, pp. 265–272, 2016, doi: 10.13700/j.bh.1001-5965.2015.0107.

[21] T. Kazama and A. Yamaguchi, "Optimum design of bearing and seal parts for hydraulic equipment," *Wear*, vol. 161, nos. 1–2, pp. 161–171, Apr. 1993.

[22] T. Kazama and A. Yamaguchi, "Application of a mixed lubrication model for hydrostatic thrust bearings of hydraulic equipment," *J. Tribol.*, vol. 115, no. 4, pp. 686–691, Oct. 1993.

[23] A. Schenk and M. Ivantysynova, "A transient thermoelastohydrodynamic lubrication model for the slipper/swashplate in axial piston machines," *J. Tribol.*, vol. 137, no. 3, Jul. 2015, Art. no. 031701.

[24] A. Schenk and M. Ivantysynova, "An investigation of the impacte of elastohydrodynamic deformation on powerloss in the slipper swashplate interface," in *Proc. 8th JRPS Int. Symp. Fluid Power*, Okinawa, Japan, 2011, pp. 228–234.

[25] U. Wieczorek and M. Ivantysynova, "Computer aided optimization of bearing and sealing gaps in hydrostatic machines—The simulation tool caspar," *Int. J. Fluid Power*, vol. 3, no. 1, pp. 7–20, Jan. 2002.

[26] H. Tang, Y. Yin, Y. Ren, J. Xiang, and J. Chen, "Impact of the thermal effect on the load-carrying capacity of a slipper pair for an aviation axial-piston pump," *Chin. J. Aeronaut.*, vol. 31, no. 2, pp. 395–409, Feb. 2018, doi: 10.1016/j.cja.2017.06.004.

[27] H. S. Tang, Y. Ren, and J. W. Xiang, "A novel model for predicting thermoelastohydrodynamic lubrication characteristics of slipper pair in axial piston pump," *Int. J. Mech. Sci.*, vols. 124–125, pp. 109–121, May 2017, doi: 10.1016/j.ijmecsci.2017.03.010.

[28] T. Hesheng, Y. Yaobao, and L. Jing, "Lubrication characteristics analysis of slipper bearing in axial piston pump considering thermal effect," *Lubrication Sci.*, vol. 28, no. 2, pp. 107–124, Mar. 2016, doi: 10.1002/ls.1304.

[29] R. M. Harris, K. A. Edge, and D. G. Tilley, "Predicting the behavior of slipper pads in swashplate-type axial piston pumps," *J. Dyn. Syst., Meas., Control*, vol. 118, no. 1, pp. 41–47, Mar. 1996.

[30] B. Xu, J. Zhang, and H. Yang, "Investigation on structural optimization of anti-overturning slipper of axial piston pump," *Sci. China Technol. Sci.*, vol. 55, no. 11, pp. 3010–3018, Nov. 2012, doi: 10.1007/s11431-012-4955-x.

[31] B. Xu and J.-H. Zhang, "Effect of case drain pressure on slipper/swashplate pair within axial piston pump," *J. Zhejiang Univ. Sci. A*, vol. 16, pp. 1001–1014, Dec. 2015, doi: 10.1631/jzus.A1500182.

[32] Q. Chao, J. Zhang, B. Xu, Q. Wang, and H. Huang, "Test rigs and experimental studies of the slipper bearing in axial piston pumps: A review," *Measurement*, vol. 132, pp. 135–149, Jan. 2019, doi: 10.1016/j.measurement.2018.09.027.

[33] S. Xia, J. Zhang, S. Ye, B. Xu, W. Huang, and J. Xiang, "A spare support vector machine based fault detection strategy on key lubricating interfaces of axial piston pumps," *IEEE Access*, vol. 7, pp. 178177–178186, 2019, doi: 10.1109/ACCESS.2019.2958141.

[34] Z. Y. Yu, Z. Y. Li, and S. D. Yang, "The problems and improvement of slipper socket in a water hydraulic piston pump," *J. Eng. Des.*, vol. 9, no. 3, pp. 116–118, 2002.

[35] Z. Y. Yu, S. L. Nie, and S. D. Yang, "Research and the application of a new style hydrostatic slipper pad in water hydraulic pump," *Hydraulic Pneumatic*, no. 10, pp. 54–56, 2002.

[36] A. Wondergem, "Piston/cylinder interface of axial piston machines—Effect of piston micro-surface shaping," M.S. thesis, Dept. Elect. Ag. Biol. Eng., Purdue Univ., West Lafayette, IN, USA, 2014.

ZEBO WANG was born in 1986. He received the M.S. degree in mechatronic engineering from the Kunming University of Science and Technology, Kuming, China, in 2012. He is currently pursuing the Ph.D. degree in mechanical engineering with the Harbin Institute of Technology, mainly engaged in modeling and optimization of hydraulic components, and computer simulation design.

JIHAI JIANG (Member, IEEE) was born in 1957. He received the Ph.D. degree in mechanical engineering from the Harbin Institute of Technology, Harbin, China, in 1999.

He is currently a Professor with the School of Mechatronics Engineering, Harbin Institute of Technology. He has conducted several projects from the National Nature Science Foundation, two projects from the National Key Technology Research and Development Program. His current research interests include new type hydraulic components, advanced design technology, energy saving technology, and reliability research of hydraulic components.

GEQIANG LI was born in 1971. He received the Ph.D. degree in mechanical engineering from the Harbin Institute of Technology, Harbin, China, in 2007. He is currently a Professor with Department of Mechanical and Electrical Engineering, Henan University of Science and Technology, Luoyang. He has conducted four projects from the National Nature Science Foundation. His current research interests include computer control and system integration technology of electro-hydraulic servo systems, and modern control theory and its application in hydraulic servo systems.

• • •